Stress Changes on the Garlock Fault During and After the 2019 Ridgecrest Earthquake Sequence

1. **Marlon D. Ramos**[1] ramosmd@umich.edu
2. **Jing Ci Neo**[1] neoj@umich.edu
3. **Prithvi Thakur**[1] prith@umich.edu
4. **Yihe Huang**[1] yiheh@umich.edu
5. **Shengji Wei**[2] shjwei@ntu.edu.sg

1. University of Michigan, Department of Earth and Environmental Sciences
2. Nanyang Technological University of Singapore, Asian School of the Environment

Abstract

The recent 2019 Ridgecrest earthquake sequence in Southern California jostled the seismological community by revealing a complex and cascading foreshock series that culminated in a M7.1 mainshock. But the central Garlock fault, despite being located immediately south of this sequence, did not coseismically fail. Instead, the Garlock fault underwent post-seismic creep and exhibited a sizeable earthquake swarm. The dynamic details of the rupture process during the mainshock are largely unknown, as is the amount of stress needed to bring the Garlock fault to failure. We present an integrated view of how stresses changed on the Garlock fault during and after the mainshock using a combination of tools including kinematic slip inversion, Coulomb stress change, and dynamic rupture modeling. We show that positive Coulomb stress changes cannot easily explain observed aftershock patterns on the Garlock fault, but are consistent with where creep was documented on the central Garlock fault section. Our dynamic model is able to reproduce the main slip asperities and kinematically estimated rupture speeds ($\leq$ 2 km/s) during the mainshock, and suggests the temporal changes in normal and shear stress on the Garlock fault were greatest near the end of rupture. The largest static and dynamic stress changes on the Garlock fault we observe from our models coincide with the creeping region, suggesting that positive stress perturbations could have caused this during or after the mainshock rupture. This analysis of near-field stress change evolution gives insight into how the Ridgecrest sequence influenced the local stress field of the northernmost Eastern California Shear Zone.

Introduction

The 2019 Ridgecrest earthquake sequence involved the rupture of a left-lateral M6.4 foreshock that occurred on July 4, and a right-lateral M7.1 mainshock that occurred on July 6 and initiated approximately 13 km northwest of the foreshock epicenter (Fig. 1a). This sequence was characterized by the activation of multiple orthogonal fault segments that are collectively referred to as the Little Lake fault zone (Llfz). Coseismic rupture of these faults continues to produce aftershocks, but it did not influence the adjacent left-lateral Garlock fault to fail. Instead, this sequence caused as much as three centimeters of surface creep on the Garlock fault that has been detected geodetically (Barnhart et al., 2019; Ross et al., 2019).

Several kinematic slip models have been developed to estimate the evolution of slip and rupture propagation during this highly complex sequence (Barnhart et al., 2019; Chen et al., 2020; Goldberg et al., 2020; Liu et al., 2019; Ross et al., 2019; Zhang et al., 2020). These models are

consistent in the respect that a majority of foreshock and mainshock slip is limited to the upper 10 km depth. Positive stress change amplitudes (~0.5 MPa) are suggested from static Coulomb modeling generally coincide with the ~25-km long region of creep on the central Garlock fault segment (Barnhart et al., 2019). But the dynamic details of rupture and how stresses were mediated by the seismic wavefield remains hazy. The Garlock fault was apparently not near critical failure, or else we would have observed coseismic rupture there as well; this implies that the stress perturbations were unable to bring shear stresses to overcome the static Garlock fault strength.

When the Garlock fault will slip again is a major unknown. The Garlock fault extends for ~260 km and is geometrically segmented into western, central, and eastern sections that are characterized by variations in geologic slip-rate and recurrence interval (Davis and Burchfiel, 1973; Hill et al., 1953, McGill and Sieh, 1991). Astiz and Allen (1983) analyzed historical seismicity on this fault and hypothesized that a rupture on the eastern Garlock segment may be more likely given its apparent seismic gap, though both the central and western sections can independently support ~M7 earthquakes. Paleoseismic evidence suggests historic, non-periodic surface rupture for the central Garlock segment (Dawson et al., 2003). During the Ridgecrest sequence, different regions of the central Garlock fault segment experienced a swarm of low-magnitude earthquakes (ML<3.2; Ross et al., 2019) and underwent creep. How the strain accumulation budget of the central Garlock fault was influenced by the recent Ridgecrest sequence is enigmatic and warrants further scrutiny for seismic hazard analysis. A spatial separation between the Ridgecrest mainshock and Garlock fault planes is furthermore subject to uncertainty, as is the possibility of rupture branching from a segment of the Garlock fault onto an adjacent segment or to the San Andreas fault during a future earthquake. In particular, the central and western segments have co-ruptured within the last 10 kya, despite a step-over structure in between them (Madugo et al., 2012). Assessing the possibility of how close the Garlock fault is to failure depends on both the static and dynamic stress perturbations from the Ridgecrest sequence.

We aim to present a physically consistent picture of the stress interaction vis-à-vis the Garlock fault during and after the Ridgecrest sequence. We draw from updated kinematic inversion results that utilize geodetic, teleseismic and near-field strong ground-motion recordings to independently constrain the fault slip amplitude, extent and rupture initiation locations of the foreshocks and M7.1 mainshock. This is then used to inform our static Coulomb stress analysis and dynamic rupture modeling efforts. Our analysis illustrates that both normal and shear stress

changes were highest on the Garlock fault at the end of mainshock rupture, and could have been responsible for the observed geodetic creep as soon as ~30 seconds from mainshock rupture initiation.

Methodology

Kinematic Slip Inversion

We use a joint slip-inversion model that is based on static GPS, teleseismic and local strong-ground motion datasets (Ji et al., 2002). The M6.4 foreshock and the M7.1 mainshock are modeled with two and single fault plane geometries, respectively (Fig. 1). Slip along the mainshock fault occurs along a 100-km long segment that dips at ~88 degrees (Fig. 1b). Of the two foreshock fault planes, one is nearly parallel to the strike of the mainshock (Plane 1), whereas the second is perpendicular to the mainshock (Plane 2; Fig. 1c, Table 1). These fault plane geometries are consistent with those estimated by the USGS and do not extend deeper than 16-km depth. Geologic mapping and Interferometric Synthetic Aperture Radar (InSAR) observations of surface-breaching rupture strands during the Ridgecrest sequence suggest that our geometries are reasonable (Kendrick et al., 2019; Xu et al., 2020). We use the slip inversion results for the foreshock and mainshock fault planes as input into our static and dynamic stress change modeling.

Static Model: Coulomb Stress-Change

Static stress changes are the final changes in the normal and shear stresses on the fault in response to slip after all seismic waves have propagated through. Such stress changes during the foreshock and mainshock of the Ridgecrest sequence have triggered thousands of aftershocks (Ross et al., 2019). Coseismic stress changes have also been known to enhance or to reduce creep after the earthquake (e.g., Allen et al., 1972, Bodin et al., 1994, Lienkaemper et al., 1997). Barnhart et al. (2019) observed that an increase in the Coulomb stress change from the Ridgecrest earthquake was correlated with the surface deformation after the earthquake. Studies have also suggested that the M6.4 foreshock and other large foreshocks promoted the rupture of the mainshock (Barnhart et al., 2019; Goldberg et al., 2020; Lozos and Harris, 2020).

To assess static stress changes, we calculate the Coulomb stress change (ΔCFS) using the Coulomb3 software (Lin and Stein 2004; Toda et al. 2005). We investigate the ΔCFS caused by the foreshock on the mainshock and separate the contribution of stress change from each of the two foreshock fault planes (Plane 1 and Plane 2; Fig 2). We use a friction coefficient of 0.6 and a

depth of 5 km for the foreshock-mainshock static stress change calculation because a majority of slip is resolved on foreshock Plane 2 (Fig. 1c), which will dominate the ΔCFS amplitude.

We also calculate the ΔCFS due to mainshock slip on the Garlock fault. We represent the Garlock fault geometry as a plane with a strike, dip and rake of 70, 90, and 0 degrees, respectively. The strike of the Garlock fault varies from 68° in the east to 84° in the west (Fig. 3), but we use 70° for the receiver fault as it is closest to the strike of the western Garlock fault segment where the cluster of aftershocks occurred. Lastly, to address uncertainty in static friction level and hypocenter depth, we also examine how varying these parameters influences our results. We compare the results from friction coefficients of 0.2, 0.4 and 0.6, and at 5 km depth, where peak slip occurred, and at 10 km depth, where the asperity with most slip extends.

Dynamic Model: Initial Conditions and Constraints

We model the mainshock fault plane as a 100-km, planar 2-D crack embedded in a homogeneous, isotropic, and linearly elastic medium with a shear-wave speed of 3.2 km/s. The model domain is composed of rectangular elements enclosed on all sides by absorbing boundaries (Fig. S1). We choose a finite element size of 600-m with four Gauss-Lobatto-Legendre nodes (NGLL) to resolve dynamic rupture propagation at seismic frequencies up to 1 Hz for consistency with that resolved by the strong-motion dataset.

We select the linear slip-weakening friction law to control fault slip evolution and utilize the 2-D spectral element code SEM2DPACK to solve for dynamic rupture propagation (Ampuero, 2009). The critical-slip distance (D_c) is 0.3 m, which is constant along the fault (except for ~15 km around the nucleation region) and is within the plausible range of previous slip-weakening dynamic rupture simulations for other crustal earthquakes of comparable magnitude and rupture dimension (e.g., Ma and Archuleta, 2006; Lozos and Harris, 2020; Tinti et al., 2009). If dynamic friction (μ_d) is below the static friction (μ_s) level, then the fault experiences a strength-drop during coseismic rupture and its frictional behavior is slip-weakening; conversely, if the dynamic friction is greater than static friction, there is no work available to grow the propagating shear crack and the frictional behavior is slip-strengthening. The static friction coefficient is 0.5 everywhere along the fault. The fault is slip-weakening (μ_d = 0.1) along the central 70 km segment (35 km southeast and northwest of hypocenter) and slip-strengthening (μ_d= 0.7) everywhere else in order to prohibit rupture from breaking the entire fault.

Given that we represent a strike-slip fault as a Mode II in-plane crack, our stress and friction conditions are relative to a region on the mainshock fault plane at depth. Our model aims to reproduce the rupture propagation along the section of the fault that crosses through the main slip asperity imaged in the kinematic inversion (Fig. 4). Effective normal stress is set to a constant level of 50 MPa that is consistent with elevated pore-pressure levels in the middle of permeable fault zones (Rice, 1992).

The initial shear stress distribution is a critical ingredient for any dynamic earthquake rupture model and determines the dynamic stress drop which in turn governs slip amplitude. We first calculate the static stress drop due to fault slip given by the kinematic inversion using a computationally efficient algorithm (Fig. 4; Ripperger and Mai, 2004). Earthquakes can exhibit total or near-total stress-drop due to strong dynamic weakening (e.g., Noda and Lapusta, 2013; Brodsky et al., 2020), meaning that the final shear stress on the fault after an earthquake is at or very near its dynamic fault strength level (the product of effective normal stress and dynamic friction). We make this assumption to calculate our initial shear stress by adding the static stress drop to the dynamic fault strength (Fig. 4).

Rupture is artificially nucleated in the middle of the fault using the time-weakening method (Andrews, 1985). This technique requires twice the critical half-crack length ($2L_c$), an effective friction level (μ_o), and a weakening time scale (T_c) after which the prescribed nucleation is turned off and rupture spontaneously evolves according to the non-linear interaction between fault strengths and stresses. Given the friction law parameters we assume for Mode II rupture in an elastic domain, $2L_c$ is given by

$$2L_c = \frac{2}{1-\nu}\frac{G}{\pi}\frac{\tau_s-\tau_d}{(\tau_o-\tau_d)^2}D_c \quad (1)$$

where G is the shear modulus (30 GPa), ν is the Poisson's ratio, τ_s is the static fault strength, τ_d is the dynamic fault strength, τ_o is the initial shear stress, and μ_o is the effective friction coefficient calculated as the ratio between initial shear and effective normal stress amplitudes at the hypocenter. We determined that a $2L_c$ of 2 km (μ_o of ~0.1) and T_c of 10 seconds are necessary to nucleate and sustain spontaneous rupture.

Results

Kinematic Slip Inversion

Using our kinematic inversion methodology, the mainshock hypocenter has been relocated to a depth of 3 km by the arrival times of nearby strong motion and broadband seismic stations

(Fig 1b). The aftershock hypocenter is deeper (9 km) and slip is distributed across two fault segments (Fig 1c). The fault parameters and hypocenters of both earthquakes are summarized in Table 1. We note that the M7.1 mainshock ruptured bilaterally with a majority of slip concentrated within the upper 10 km and a peak slip amplitude of 4.7 m located ~10 km NW of the hypocenter (Fig. 1b). There is a smaller asperity that underwent ~ 2.5 m of slip SE of the mainshock hypocenter, as well. On the other hand, peak slip resolved for the foreshock is lower (1.3 m) and occurred mostly on Plane 2, which is perpendicular to the mainshock fault plane (1c).

We also compare our mainshock slip inversion results to those from other studies of the Ridgecrest mainshock. We utilize seismic and GPS datasets to constrain the slip which is similar to the approach by Liu et al., (2019). In contrast, other studies make use of a combination of seismic, high-rate GPS and InSAR (Chen et al., 2020; Goldberg et al., 2020; Ross et al., 2019), InSAR and optimal image-tracking (Barnhart et al., 2019), or only seismic datasets (Zhang et al., 2020). The details of slip distribution, and in particular the relative location and amplitude of maximum slip, varies between studies. The maximum slip is mostly shallower (~4 km, Barnhart et al., 2019), to the northwest of (~10 km, Liu et al., 2019), or slightly deeper (~5 km, Ross et al., 2019) than the hypocenter location used in their inversion. The kinematic slip inversion we present resolves two primary slip patches (i.e., Fig. 1), which have similar amplitudes (4.7 m and 2.5 m) and locations (northwest and southeast of hypocenter) to the Barnhart et al., (2019), Liu et al., (2019), and Zhang et al., (2020) inversion results. A major difference in maximum slip amplitude occurs between our model and the Ross et al., (2019) study, which estimates as much as nine meters of slip between 5 and 10 km depth. Other notable changes between our study and other's include a more widely distributed higher (> 4 m) slip distribution (Chen et al., 2020), or a maximum slip amplitude difference on the order of 1.5 meters between what is resolved from our inversion (4.7 m) and the Goldberg et al., (2020) [~3.5 m] study. Such differences are most likely due the datasets used to constrain the inversions as well as the particular inversion parameterization. Overall, our mainshock slip distribution is consistent with other published models, characterized by bilateral rupture propagation and a shallow (< 10 km) slip distribution.

Static Stress Change

We find the foreshock increased the ΔCFS near the edges of the foreshock faults, especially at the intersection of Plane 2 and mainshock fault, but our relocated mainshock hypocenter is located in a region of slightly decreased ΔCFS (Fig. 2a, S2). However, this result depends on the

method used to locate the mainshock hypocenter and its uncertainty. For instance, the Advanced National Seismic System Comprehensive Catalog (ANSS) epicentral coordinates agree with ours to within a kilometer but its depth is 5 km deeper than our preferred depth of 3 km, whereas the hypocenter resolved by Ross et al. (2019) is ~12 km away from the foreshock hypocenter but at a similar shallow depth (< 4 km). The hypocenters estimated by the ANSS catalog and by Ross et al. (2019) are located near the edges of different regions of positive ΔCFS. We also calculated the ΔCFS from both foreshock planes separately (Fig. 2b, c). Plane 2 has a much larger slip compared to Plane 1, with almost twice the peak slip (i.e., 1.3 versus 0.74 m; Table 1). However, Plane 1 causes a ~0.5 MPa greater ΔCFS on the southeast region of the mainshock fault compared to Plane 2, as Plane 1 is closer (Fig. 2b). This underscores the sensitivities of the ΔCFS to input fault slip amplitude and extent.

We further calculate the ΔCFS on the Garlock fault due to mainshock slip and assess the effect of various friction coefficients and depths on our results. Overall, we find that the friction coefficient has a relatively small (i.e., a difference within ~ 0.1 MPa) impact on our ΔCFS results for a given depth (Fig. 3). Larger friction coefficients tend to increase the ΔCFS amplitude and changes the spatial distribution of positive and negative stress changes (Fig. 3). This is similar to Barnhart et al. (2019), where they found that their results are consistent for all friction coefficients that they tested. For a given friction coefficient, changing the depth of the ΔCFS calculation from 5 km to 10 km increases the ΔCFS amplitude by ~0.3 MPa and decreases the extent of the region of positive ΔCFS on the Garlock fault by approximately 20 km (Fig. 3). The amplitude difference is because the largest portion of mainshock slip extends to about 10 km depth, and the change in slip at this depth produces a larger ΔCFS than at 5 km depth. The region of positive ΔCFS in proximity to the creeping section of the Garlock fault is most consistent in spatial extent with that of Barnhart et al. (2019) when we use a friction coefficient of 0.2 and a depth of 5 km. Lastly, we find that the cluster of aftershocks on the Garlock fault are unlikely to be simply explained by ΔCFS from the mainshock as the value of the stress change can be small (< 0.01 MPa) or even negative (~ -0.1 MPa) [Fig. 3].

Dynamic Earthquake Rupture model

Our first goal is to explain the kinematic fault slip distribution using rupture dynamics. We seek to reproduce the two primary patches of 2.5 m and 4.7 m slip southeast and northwest of the

hypocenter, respectively, (Fig. 1b; 5a). We show the rupture history until 35 seconds to highlight the arrest of both the northwest and southeast rupture fronts (Fig. 5).

The initial conditions and friction parameters outlined in the methods section gives a good agreement between the kinematically imaged and dynamically modeled slip distributions. The exception is the region near the hypocenter, where the dynamic rupture model overpredicts the kinematic slip amplitude by ~0.8 meters (Fig. 5a). This is most likely due to our time-weakening nucleation procedure, but is probably within the uncertainty of the true fault slip resolved by the kinematic inversion. The distribution in dynamic stress drop is positive where higher slip is concentrated, and negative in a small region southeast of the hypocenter and where we impose slip-strengthening frictional behavior at the ends of the fault (Fig. 5b).

The bilateral mainshock dynamic rupture is overall heterogeneous and spatiotemporally complex (Fig. 5c). There are three major asperities (i.e., relatively high dynamic stress-drop regions) that contribute to several rupture-front accelerations (Fig. 5b, c). The model shows a slow (< 1 km/s) rupture front propagating to the southeast for the first five seconds after nucleation ceases; this southeast rupture front then accelerates to ~1.3 km/s before decelerating and arresting at 28 seconds (Fig. 5c). In contrast, the northwest rupture front propagates at a more uniform speed (~2.1 km/s) before decelerating and stopping at ~25 seconds. These rupture speeds are consistent with recent kinematic models that prescribe a constant sub-Rayleigh mainshock rupture speed (Goldberg et al., 2020; Liu et al., 2019; Ross et al., 2019; Zhang et al., 2020). Rupture speed depends on how much total available energy is partitioned into radiated or fracture energy during the faulting process. Slower ruptures (as observed during the Ridgecrest sequence) may be due to a relatively high fracture energy consumed on the fault, consistent with the hypothesis that the Llfz is less compliant and more energy was needed to break multiple fault segments (Goldberg et al., 2020; Liu et al., 2019; Perrin et al., 2016). Our dynamic model shows that the mainshock rupture fronts do not exhibit slip-rate amplitudes above 4 m/s and propagate at well below the Rayleigh wave speed.

Temporal Stress Changes on the Garlock fault

Using our dynamic rupture model, we investigate the stress contributions to a section of the central Garlock fault during and after the Ridgecrest mainshock. Note that given the limitation of our modeling domain, we cannot assess far-field dynamic stress contributions from

surface-wave amplitude changes. We instead focus on how the initial peak stresses carried by near-field seismic waves impacted the Garlock fault during coseismic rupture.

The 2-D stress tensor in our model is for an isotropic body and yields three unique components: σ_{xx}, σ_{yy}, and σ_{xy}. Only one component of the normal stress (σ_{yy}) and the shear stress (σ_{xy}) are important to be considered further in our analysis. If we place the strike of the mainshock fault plane on an east-west coordinate system, the angle between the mainshock and Garlock fault planes (measured clockwise) is approximately 110 degrees. We therefore applied a rotation of the stress field at a particular instant in time to represent the stress perturbation the mainshock imparts to the Garlock fault (Fig. 6; see Supplemental Information). When this rotation is performed at the final time-step, the rotated stress field is equivalent to the static stress change on the Garlock fault. We observe an abrupt transition from negative to positive normal static stress change as one crosses the intersection of the strike of the mainshock fault plane (Fig. 7a). The shear stress change is slightly more complex with an asymmetric stress amplitude distribution across the fault, but shows a very pronounced region of positive stress change that generally coincides with the ~25-km long section of the central Garlock fault that underwent creep (Fig. 7b; Barnhart et al., 2019; Xu et al., 2019). To confirm our static stress change analysis from the dynamic model, we compare it to our ΔCFS calculation and find that its orientation and amplitude are consistent (Fig. S4).

We also calculate the temporal stress change on the central Garlock fault segment during the Ridgecrest mainshock. We select one point near the creeping region on the Garlock fault (-60 km, -10 km; Fig. 7 and Fig. 8) to show how normal and shear stresses change during mainshock rupture. While propagation spontaneously arrests at near ~28 seconds towards the southeast, we simulate rupture until 100 seconds to make sure stress changes relax to constant levels, which are attained at 60 seconds (Fig. 9). This section of the central Garlock fault begins to experience a positive normal stress change near 17.5 seconds (Fig. 7). During the main portion of coseismic rupture, normal stress changes reach their maximum of ~0.3 MPa at 32 seconds (Fig. 7f, 9a). In contrast, positive shear stress changes arrive at the Garlock fault in three distinct pulses (e.g., Fig. 8f, 9a). Two of these positive shear stress change pulses arrive after the largest change in normal stress change and continue to be above the normal stress change amplitude for the remainder of our simulation (Fig. 8, 9a). The extrema of the normal and shear stress change amplitudes are symmetric through time due to the alternating arrivals of compressional (P) and shear (SV) wave motions.

Discussion and Conclusion

We show that stress changes during and after the Ridgecrest foreshocks and mainshock may have influenced post-seismic creep on the central Garlock fault segment and brought certain regions potentially closer to coseismic failure. Our results also shed light on the temporal stress evolution on the Garlock fault due to source dynamics. Because both normal and shear stresses vary during coseismic rupture, evaluating their respective contribution is of critical importance to identifying periods when stresses changes may have been favorable to engender the observed post-seismic creep.

The Coulomb stress change results show that positive static stress changes were experienced on the central Garlock fault due to mainshock slip (Fig. 3) and are coincident with previously documented fault creep (Barnhart et al., 2019; Ross et al., 2019; Xu et al., 2020). Among Coulomb stress changes calculated for different friction levels and depths, in only one case (i.e., friction level of 0.6) is a positive static stress change on the order of ~0.1 MPa observed adjacent to the region of the Garlock fault that experienced a sizeable aftershock swarm (Fig. 3). This may indicate that other post-seismic relaxation processes or dynamic stress changes were at play to produce this aftershock pattern. Various studies have also calculated the Coulomb stress change of the foreshock at the mainshock hypocenter with their slip inversion results. While Barnhart et al (2019) found an increase in Coulomb stress change of 0.6 MPa due to the foreshock at their hypocenter, Zhang et al. (2020) found an increase of 0.04 MPa and Goldberg et al. (2020) found a <0.1 MPa increase. we find that a 0.1 MPa decrease in Coulomb stress change at the location of our hypocenter. The disparity in magnitude and sign of the results may be due to the fact that Coulomb stress calculations are very sensitive to the slip inversion model used and the inferences may change depending on the location of the hypocenter, as well.

When we assess the ΔCFS through time we find that ΔCFS predominantly increases during mainshock rupture and remains at a high level afterwards; this is evident from our dynamic model as the normal stress change amplitude is mostly below the shear stress amplitude (Fig. 9b). Temporal stress changes during the mainshock rupture also support predominantly positive shear stress changes near this creeping Garlock region (Fig. 8), whereas positive and negative normal stress distributions are observed on both sides of the projected intersection of the mainshock and Garlock fault planes (Fig. 7). Our results for temporal normal and shear stress changes near the Garlock fault agree with other dynamic rupture simulations that prescribe a complex 3-D fault

geometry, but similar constitutive friction law parameters (Lozos and Harris, 2020). Moreover, this study also documents a detailed temporal evolution of normal, shear, and Coulomb stresses impacting the central Garlock fault (i.e., Fig. 9), and not just the final stress changes after all seismic waves have been radiated away. Because positive normal stress changes serve to strengthen the fault whereas positive shear stresses should bring the fault closer to failure, our dynamic model offers one possible scenario that creep could have occurred as soon as ~15 seconds after nucleation of the Ridgecrest mainshock when positive shear stresses began to arrive at the Garlock fault. However, this is speculative given that we do not have information on the absolute stress state of the Garlock fault prior to the aftershock/mainshock sequence.

Our dynamic model also suggests that the largest shear stress changes (0.3 – 0.4 MPa) arrived before and after the largest normal stress changes, but they are comparable in amplitude (Fig. 7, 8, 9a). Given this maximum shear stress change amplitude at a given time, we estimate approximately 0.1 centimeters of slip may have been triggered near the creeping section of the Garlock fault at a depth less than 1 km (Fig. S5a). We also test a model where creep on the Garlock fault was exceptionally shallow (< 300 m depth; Schleicher et al., 2019) but the distribution of creep is more heterogeneous. We still obtain a similar amount of creep that is consistent with the shear stress change amplitude (Fig. S5b). These estimates are lower than the maximum magnitude of resolved surface creep (i.e., ~3 cm) documented earlier by Barnhart et al., (2019) and Ross et al., (2019), however. The creep magnitudes we estimate are furthermore only valid for a homogenous, Poisson solid and should be considered an upper-bound for any given shear stress-change perturbation because our dynamic rupture model captures the region on the mainshock fault plane that experiences the greatest dynamic stress-drop (~7 MPa; Fig. 5b). There is potential for more creep to be accommodated by successive near-field stress changes arriving at the Garlock fault during mainshock rupture, but this depends on the near-surface rheology and earthquake history of the central Garlock fault. Additionally, we cannot rule out the possibility that the maximum resolvable creep was driven by cumulative or post-seismic strain-rate changes not seen by satellite observations since the smallest observation window is at least five to six days after the mainshock (Barnhart et al., 2019). But extensometer data imply that it did not extend very deep into the crust, regardless of how much triggered creep was (Bilham and Castillo, 2020).

The fact that the Garlock fault did not coseismically fail could be supported by theoretical considerations to the prestress state, rupture speed and fault orientation between the mainshock

and Garlock fault planes if they are connected (Poliakov et al., 2002; Kame et al., 2003). For a low angle of maximum horizontal shear stress (SH_max) with respect to the fault (< 45 degrees), this prestress state encourages rupture to bifurcate towards the compressional side, whereas a higher angle (> 45 degrees) predicts that the rupture along the extensional side is more favorable (Poliakov et al., 2002). Yang and Hauksson (2013) inverted earthquake focal mechanisms in central and southern California, estimating the regional SH_max orientation lies between zero and five degrees east of North. Our dynamic rupture model predicts an average mainshock rupture-front to shear-wave speed ratio of 0.4. Given that the mainshock fault plane is approximately oriented 45 degrees west of North, such a low prestress orientation together with low rupture speed levels are not likely to encourage rupture propagation to the Garlock fault, if connected (Kame et al., 2003). This mechanical argument, however, must be taken with a grain of salt considering changes in the local stress field orientation surrounding the M7.1 mainshock due to the M6.4, smaller foreshocks, and other seismicity. A detailed seismological analysis of foreshock and aftershock stress-tensor inversions will undoubtedly place stronger constraints on the SH_max orientation to the mainshock fault plane, and perhaps lend credence to theoretical expectations we have briefly discussed here.

One aspect we could continue to explore in greater detail is how a fully dynamic model incorporating segmented foreshock and mainshock fault planes changes the details of the temporal stress changes on the Garlock fault. Several kinematic studies are able to fit seismogeodetic data using a segmented fault model (e.g., Goldberg et al., 2020; Liu et al., 2019; Ross et al., 2019). Given that the Ridgecrest sequence produced multiple orthogonal faulting with some ruptures breaking the surface while others not (Ross et al., 2019), we would expect the temporal stress change to accordingly reflect this complexity. We note that the geometrically segmented 3-D dynamic fault model by Lozos and Harris (2020) yields static normal and shear stress changes on the Garlock fault that are consistent to first-order in sign and amplitude with our modelling efforts. There are small differences, but this is expected due to different initial stress parameterizations, velocity structure, and fault geometry for the mainshock and foreshock fault planes.

How the M6.4 foreshock and M7.1 mainshock Ridgecrest sequences changed the local stress field in Southern California is a crucial question to consider given the proximity of these events to other active faults (e.g., Garlock and San Andreas). Through a unique combination of kinematic, static, and dynamic modeling, we present a physically coherent picture of the stress

changes on the central Garlock fault during and after the coseismic rupture of the M7.1 event. We find that positive stress changes near the creeping section of the Garlock fault are observed during and after coseismic rupture. We also show that the greatest shear stress change was comparable to the greatest normal stress change, but arrived earlier during dynamic rupture; this may have promoted a section of the Garlock fault to creep even before the Ridgecrest mainshock finished slipping. Our dynamic models physically explain the resolved slip amplitude through the mainshock hypocenter and reproduce the low sub-Rayleigh rupture speeds previously suggested by kinematic rupture models.

Data and Resources

Static stress calculations are conducted using the Coulomb 3 software available from the USGS website, https://earthquake.usgs.gov/research/software/coulomb/. All codes used in dynamic model post-processing and figure creation as well as model input and output files are archived and freely accessible on UM Deep Blue (https:// deepblue.lib.umich.edu/). Data used in the kinematic inversion are available upon request to Dr. Shengji Wei (shjwei@ntu.edu.sg). Some figures in this paper were generated with MATLAB™ software or used colormap schemes from Crameri (2018, http://doi.org/10.5281/zenodo.1243862). Within the Supplemental Material, we provide information on how we rotate stresses to the Garlock fault and show additional stress change calculations.

Acknowledgements

We thank guest editor Zachary Ross and two anonymous reviewers for their constructive comments that improved this manuscript. This study was supported by the University of Michigan. M.D. Ramos, J. C. Neo, P. Thakur and Y. Huang acknowledge the funding support from the National Science Foundation through grant awards 1663769 and 1943742. M. D. Ramos thanks P. M. Mai for providing a computationally efficient algorithm for static stress change on faults due to kinematic slip.

446

447

448 **References**

449 Allen, C. R., Wyss, M., Brune, J. N., Grantz, A., and Wallace, R. E. (1972). Displacements on the
450 Imperial, Superstition Hills, and San Andreas faults triggered by the Borrego Mountain
451 earthquake, in The Borrego Mountain Earthquake of April 9, 1968. *U.S. Geol. Sur. Profess.*
452 *Paper,* 787, 87-104.
453
454 Ampuero, J. P. (2009). SEM2DPACK: A spectral element method tool for 2D wave propagation
455 and earthquake source dynamics, User's Guide, version 2.3.6. Retrieved from
456 http://www.sourceforge.net/projects/sem2d/
457
458 Andrews, D. J. (1985). Dynamic plane-strain shear rupture with a slip-weakening friction law
459 calculated by a boundary integral method. *Bull. Seismo. Soc. Of Amer*., 75(1), 1–21.
460
461 Astiz, Luciana, Allen, C. R. (1983). Seismicity of the Garlock fault, California. *Bull. of the Seismo.*
462 *Soc. of Amer.*, 73(6), 1721–1734. https://doi.org/10.1017/CBO9781107415324.004
463
464 Barnhart, W. D., Hayes, G. P., & Gold, R. D. (2019). The July 2019 Ridgecrest, California,
465 Earthquake Sequence: Kinematics of Slip and Stressing in Cross-Fault Ruptures. *Geophys.*
466 *Res. Lett.*, (July), 859–867. https://doi.org/10.1029/2019GL084741
467
468 Bilham, R., and B. Castillo (2020). The July 2019 Ridgecrest, California, Earthquake Sequence
469 Recorded by Creepmeters: Negligible Epicentral Afterslip and Prolonged Triggered Slip
470 at Teleseismic Distances, *Seismol. Res. Lett*. XX, 1–14, doi: 10.1785/0220190293.
471
472 Bodin, P. and Gomberg, J. (1994). Triggered Seismicity and Deformation between the Landers,
473 California, and Little Skull Mountain, Nevada, Earthquakes. *Bulletin of the Seismological*
474 *Society of America*, 84, 3, 835-843.
475
476 Brodsky, E. E., Mori, J. J., Anderson, L., Chester, F. M., Conin, M., Dunham, E. M., … Yang, T.
477 (2020). The State of Stress on the Fault Before, During, and After a Major Earthquake.
478 *Annu. Rev. Earth Planet. Sci*, 48(1), annurev-earth-053018-060507.
479 https://doi.org/10.1146/annurev-earth-053018-060507
480
481 Dawson, T. E., McGill, S. F., & Rockwell, T. K. (2003). Irregular recurrence of paleoearthquakes
482 along the central Garlock fault near El Paso Peaks, California. *Jour. of Geophys. Res: Solid*
483 *Earth*, 108(B7). https://doi.org/10.1029/2001jb001744

484 Goldberg, D. E., Melgar, D., Sahakian, V. J., Thomas, A. M., Xu, X., Crowell, B. W., & Geng, J.
485 (2020). Complex Rupture of an Immature Fault Zone: A Simultaneous Kinematic Model
486 of the 2019 Ridgecrest, CA Earthquakes. *Geophysical Research Letters*, *47*(3), 1–10.
487 https://doi.org/10.1029/2019GL086382

Hill, M. L. and T W. Dibblee (1953). San Andreas, Garlock and Big Pine faults, California, Bull. *Geol Soc Am*, 64, 443-458.

Ji, C., D.J. Wald, and D.V. Helmberger (2002). Source description of the 1999 Hector Mine, California earthquake; Part I: Wavelet domain inversion theory and resolution analysis, *Bull. Seism. Soc. Am.*, Vol 92, No. 4. pp. 1192-1207.

Kame, N., Rice, J. R., & Dmowska, R. (2003). Effects of prestress state and rupture velocity on dynamic fault branching. *Jour. of Geophys. Res: Solid Earth*, 108(B5), 1–21. https://doi.org/10.1029/2002jb002189

Kendrick, K. J. et al., Southern California Earthquake Center Annual Meeting Proceedings (SCEC, 2019), contribution 9779.

King, G. and J. Nabelek, (1985). The role of fault bends in the initiation and termination of earthquake rupture. *Science*, 228, 984-987.

Lienkaemper, J. J., Galehouse, J. S., Simpson, R. W. (1997). Creep response of the Hayward fault to stress changes caused by the Loma Prieta earthquake. *Science,* 276, 5321, 2014-2016. DOI: 10.1126/science.276.5321.2014

Lin, J. and R.S. Stein (2004). Stress triggering in thrust and subduction earthquakes, and stress interaction between the southern San Andreas and nearby thrust and strike-slip faults. *J. of Geophys. Res.,* 109, B02303, doi:10.1029/2003JB002607.

Liu, C., Lay, T., Brodsky, E. E., Dascher-Cousineau, K., & Xiong, X. (2019). Coseismic Rupture Process of the Large 2019 Ridgecrest Earthquakes From Joint Inversion of Geodetic and Seismological Observations. *Geophys. Res. Lett*. https://doi.org/10.1029/2019GL084949

Lozos, J. C., & Harris, R. A. (2020). Dynamic Rupture Simulations of the M6 . 4 and M7 . 1 July , 2019 Ridgecrest , California Earthquakes. *Geophysical Research Letters*, 1–16. https://doi.org/10.1029/2019GL086020

Ma, S. and Archuleta, R.J., (2006). Radiated seismic energy based on dynamic rupture models of faulting, *J. Geophys. Res*., 111, doi:10.1029/2005JB004055.

Madugo, C. M., Dolan, J. F., & Hartleb, R. D. (2012). New paleoearthquake ages from the western Garlock fault: Implications for regional earthquake occurrence in Southern California. *Bull. of the Seismo. Soc. of Amer.*, 102(6), 2282–2299. https://doi.org/10.1785/0120110310

McGill, S. F., and K. Sieh (1991). Surficial offsets on the central and eastern Garlock fault associated with prehistoric earthquakes, *J. Geophys. Res*., 96, 21,597–21,621.

Noda, H., and N. Lapusta (2013). Stable creeping fault segments can become destructive as a result of dynamic weakening, *Nature*, 493, 518–521, doi:10.1038/nature11703.

Perrin, C., Manighetti, I., Ampuero, J.-P., Cappa, F., & Gaudemer, Y. (2016). Location of largest earthquake slip and fast rupture controlled by along-strike change in fault structural maturity due to fault growth. *Jour. of Geophys. Res: Solid Earth*, 121(5), 3666–3685. https://doi.org/10.1002/2015JB012671

Poliakov, A. N. B., Dmowska, R., & Rice, J. R. (2002). Dynamic shear rupture interactions with fault bends and off-axis secondary faulting. *Jour. of Geophys. Res*., 107(B11), ESE 6-1-ESE 6-18. https://doi.org/10.1029/2001jb000572

Rice, J. R. (1992). Fault Stress States, Pore Pressure Distributions, and the Weakness of the San Andreas Fault. *Inter. Geophys*., 51(C), 475–503. https://doi.org/10.1016/S0074-6142(08)62835-1

Ripperger, J., & Mai, P. M. (2004). Fast computation of static stress changes on 2D faults from final slip distributions. *Geophy. Res. Lett*., 31(18), 2–5. https://doi.org/10.1029/2004GL020594

Ross, Z. E., Idini, B., Jia, Z., Stephenson, O. L., Zhong, M., Wang, X., … Moore, A. W. (2019). 2019 Ridgecrest earthquake sequence. Science, 3665(October), 346–351.

Schleicher, L. S., Huang, M., Allison, K. L., and Anderson, R. J. (2019). Seismic hazard implications of post-seismic deformation and stress transfer from the 2019 Searles Valley California Earthquakes, Abstract S41C-08 presented at 2019 Fall Meeting, AGU, San Francisco, CA, 9-14 Dec., 2019.

Toda, S., R. S. Stein, K. Richards-Dinger and S. Bozkurt (2005). Forecasting the evolution of seismicity in southern California: Animations built on earthquake stress transfer. *J. Geophys. Res*., 110, B05S16, doi:10.1029/2004JB003415.

Tinti, E., Cocco, M., Fukuyama, E., & Piatanesi, A. (2009). Dependence of slip weakening distance (Dc) on final slip during dynamic rupture of earthquakes. *Geophys. Jour. Int*., 177(3), 1205–1220. https://doi.org/10.1111/j.1365-246X.2009.04143.x

Xu, X., D. T. Sandwell, and B. Smith-Konter (2020). Coseismic Displacements and Surface Fractures from Sentinel-1 InSAR: 2019 Ridgecrest Earthquakes, Seismol. Res. Lett. XX,1–7, doi: 10.1785/ 0220190275.

Yang, W. and Hauksson, E., (2013). The tectonic crustal stress field and style of faulting along the Pacific North America Plate boundary in Southern California*, Geophys. Jour. Int*., 194, 100-117, doi: 10.1093/gji/ggt113

Zhang, Y., X. Zheng, Q. Chen, X. Liu, X. Huang, Y. Yang, Q. Xu, and J. Zhao (2020). Automatic Inversion of Rupture Processes of the Foreshock and Mainshock and Correlation of the Seismicity during the 2019 Ridgecrest Earthquake Sequence, Seismol. Res. Lett. XX, 1–11, doi: 10.1785/0220190343.

578
579
580 **Author Mailing Addresses**
581 1. Marlon D. Ramos, Jing Ci Neo, Prithvi Thakur, Yihe Huang
582 2. Shengji Wei
583
584 Authors one through four may be contacted at:
585
586 Department of Earth and Environmental Sciences
587 University of Michigan
588 Room 2534
589 Attn: Marlon D. Ramos, Jing Ci Neo, Prithvi Thakur, Yihe Huang
590 1100 North University Avenue
591 Ann Arbor, MI 48109-1005
592 Author five may be contacted at:
593 Earth Observatory of Singapore
594 Nanyang Technological University
595 Attn: Wei Shengji
596 N2-01A-08
597 50 Nanyang Ave, Singapore 639798
598
599
600
601
602
603 **List of Tables**
604
605
606 **Table 1**
607 Coulomb stress-change parameters of the mainshock and aftershock fault planes. Hypocenter
608 location (latitude, longitude, depth) and maximum slip amplitude (meters) from the kinematic
609 inversion are also listed.
610

	M_w	Hypocenter	Strike	Dip	Rake	Peak Slip (m)
Mainshock	7.1	35.772N -117.602E 3 km	322	81	-170	4.7
Foreshock	6.4	35.705N -117.506E 9 km	318 228	88 81	-172 0	1.3 0.74

611
612
613
614
615
616
617

618
619
620 **List of Figure Captions**
621
622 **Figure 1.** 2019 Ridgecrest Earthquake Sequence. (a) Study area with foreshock and mainshock
623 fault planes denoted by solid lines. The approximate region of the central Garlock fault that
624 experienced creep during this sequence is indicated by the box. (b) Mainshock slip-inversion
625 results where we determine a hypocenter depth of 3 km and a peak slip amplitude of 4.7 m that is
626 immediately northwest of the hypocenter. (c) Foreshock slip-inversion results. Foreshock planes
627 parallel and perpendicular to the mainshock fault plane are denoted as Plane 1 and Plane 2,
628 respectively. Note that a northwest-southeast fault orientation is the same for the mainshock and
629 foreshock fault planes. Stars indicate epicenter (a) or hypocenter (b and c) locations. The color
630 version of this figure is available only in the electronic edition.
631
632 **Figure 2.** Coulomb stress-change due to foreshock Planes 1 and 2 on the mainshock fault plane
633 calculated at a depth of 5 km and with a friction coefficient of 0.6. (a) The combined effect of both
634 aftershock fault plane slip on the mainshock. (b) The Coulomb stress change from Plane 1 which
635 is parallel to the main fault plane. (c) Coulomb stress change from Plane 2,which is the NE-SW
636 striking cross-fault. The aftershocks depicted are the earthquakes that occurred after the foreshock
637 and do not include those induced from mainshock stress changes. The color version of this figure
638 is available only in the electronic edition.
639
640 **Figure 3**. Coulomb stress change of the mainshock on a receiver fault of 70° strike and 90° dip,
641 approximating the leftmost part of the Garlock fault in this figure. Top: Coulomb stress-change
642 results for a 5 km depth source at friction coefficients of (left to right) 0.2, 0.4, and 0.6. Bottom:
643 Coulomb stress-change results for a 10 km depth source with the same friction coefficients. The
644 color version of this figure is available only in the electronic edition.
645
646 **Figure 4**. Static stress-drop (top) and initial shear stress (bottom) along the mainshock fault
647 plane. Static stress-drop is calculated assuming a homogeneous, Poisson medium and initial
648 shear stress is computed using the complete stress-drop assumption. We select an initial shear
649 stress profile through the main asperity at 3 km depth (dashed line) as a starting condition for our
650 2-D dynamic rupture models.
651
652 **Figure 5**. (a) Along-fault slip distribution resolved by the kinematic slip inversion (solid line) and
653 that calculated from the dynamic rupture model (dashed line). The x-axis measures distance from
654 where the earthquake is nucleated in our model. (b) Dynamic stress-drop along the fault. Location
655 shown in Figure 4. (c) Spatiotemporal and bilateral rupture history predicted by the dynamic
656 rupture model. Solid lines signify average rupture front speed. Both rupture fronts propagate at
657 sub-Rayleigh wave speed.

658
659 **Figure 6**. Static stress-change field in the modeling domain rotated to the strike of the Garlock
660 fault. (a) normal stress and (b) shear stress. Garlock fault trace (dashed line) and Ridgecrest
661 mainshock fault (solid line) are superimposed onto the figure. Box denotes approximate location

of the creeping region (Barnhart et al., 2019). Spatial orientation is the same for figures 6 – 8. The color version of this figure is available only in the electronic edition.

Figure 7. Normal stress changes (σ_{yy}) at various moments in time on the central Garlock fault during coseismic rupture of the mainshock. A point on the Garlock is selected to visualize the stress amplitude variability (solid circle). Subfigures (a) through (e) represent σ_{yy}) from 17.5 to 50 seconds during rupture propagation. (f) shows the time-history of σ_{yy} where the blue squares denote the amplitude change at each of the normal stress snapshots (a-e).

Figure 8. Similar to Fig. 9, but shear stress changes (σ_{xy}) during coseismic rupture. σ_{xy} exhibits three distinct peaks in its temporal stress-change on the Garlock fault at ~28, 38, and 50 seconds.

Figure 9. Stress change evolution on a section of the Garlock fault during the entire Ridgecrest earthquake simulation. (a) Normal ($\sigma\ yy$) and shear ($\sigma\ xy$) stress change. (b) Temporal Coulomb stress change for friction coefficient levels assessed in the static stress change analysis. Note that we plot the temporal stress change starting at 10 seconds because this is when the nucleation procedure ceases.

Figures

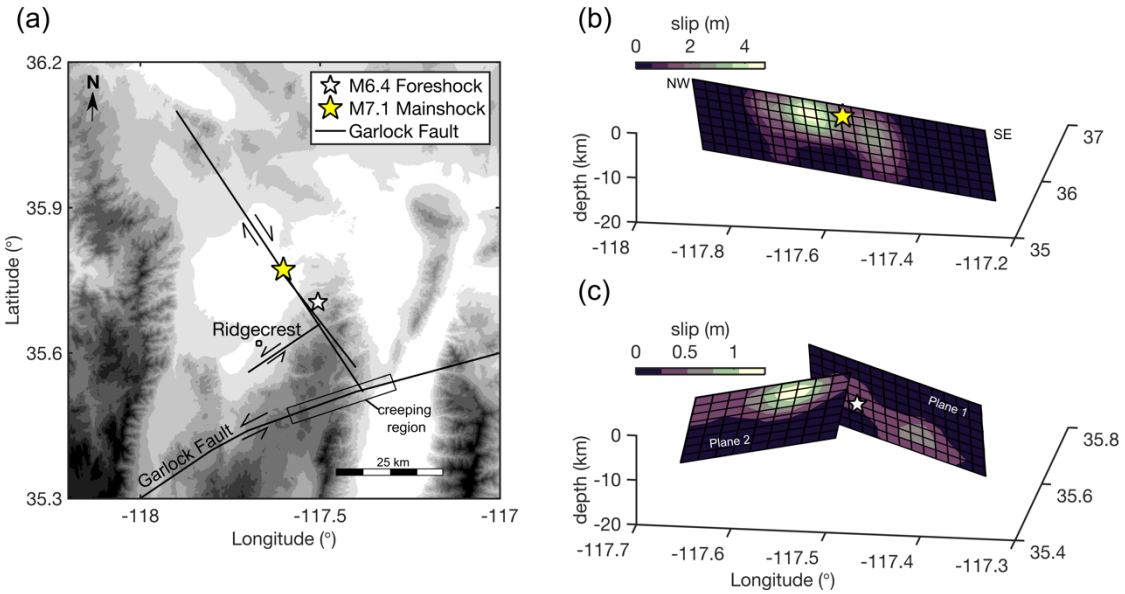

Figure 1. 2019 Ridgecrest Earthquake Sequence. (a) Study area with foreshock and mainshock fault planes denoted by solid lines. The approximate region of the central Garlock fault that experienced creep during this sequence is indicated by the box. (b) Mainshock slip-inversion results where we determine a hypocenter depth of 3 km and a peak slip amplitude of 4.7 m that is immediately northwest of the hypocenter. (c) Foreshock slip-inversion results. Foreshock planes parallel and perpendicular to the mainshock fault plane are denoted as Plane 1 and Plane 2, respectively. Note that a northwest-southeast fault orientation is the same for the mainshock and foreshock fault planes. Stars indicate epicenter (a) or hypocenter (b and c) locations. The color version of this figure is available only in the electronic edition.

726

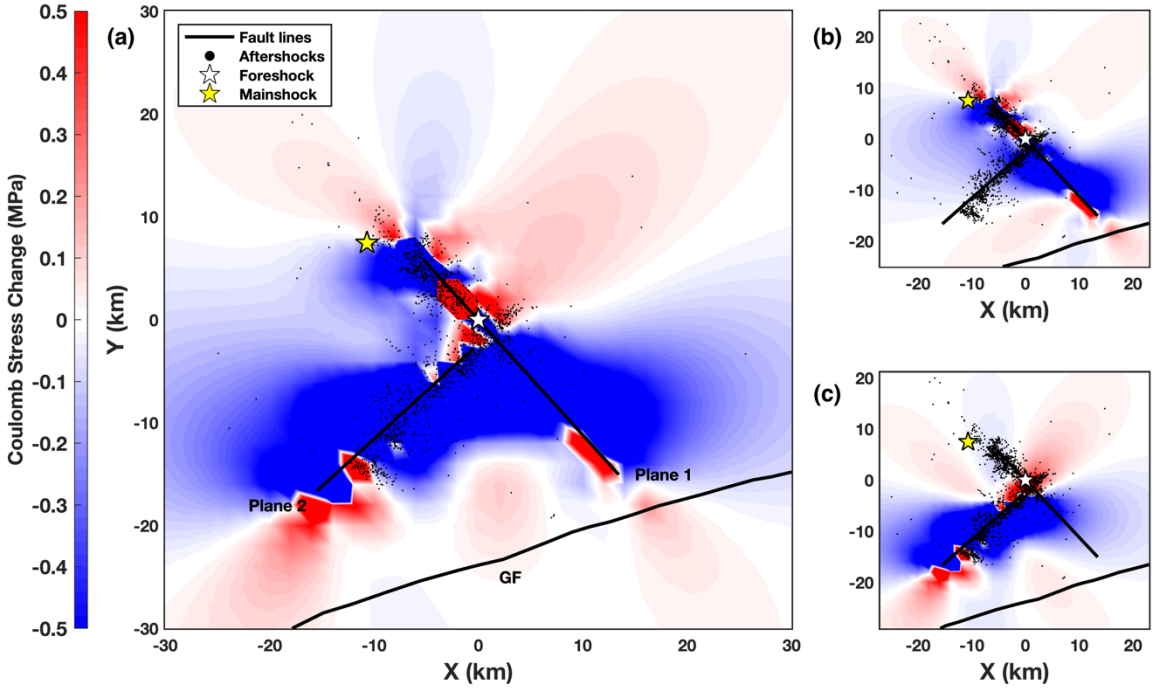

727
728 **Figure 2.** Coulomb stress-change due to foreshock Planes 1 and 2 on the mainshock fault plane
729 calculated at a depth of 5 km and with a friction coefficient of 0.6. (a) The combined effect of both
730 aftershock fault plane slip on the mainshock. (b) The Coulomb stress change from Plane 1 which
731 is parallel to the main fault plane. (c) Coulomb stress change from Plane 2, which is the NE-SW
732 striking cross-fault. The aftershocks depicted are the earthquakes that occurred after the foreshock
733 and do not include those induced from mainshock stress changes. The color version of this figure
734 is available only in the electronic edition.
735
736
737

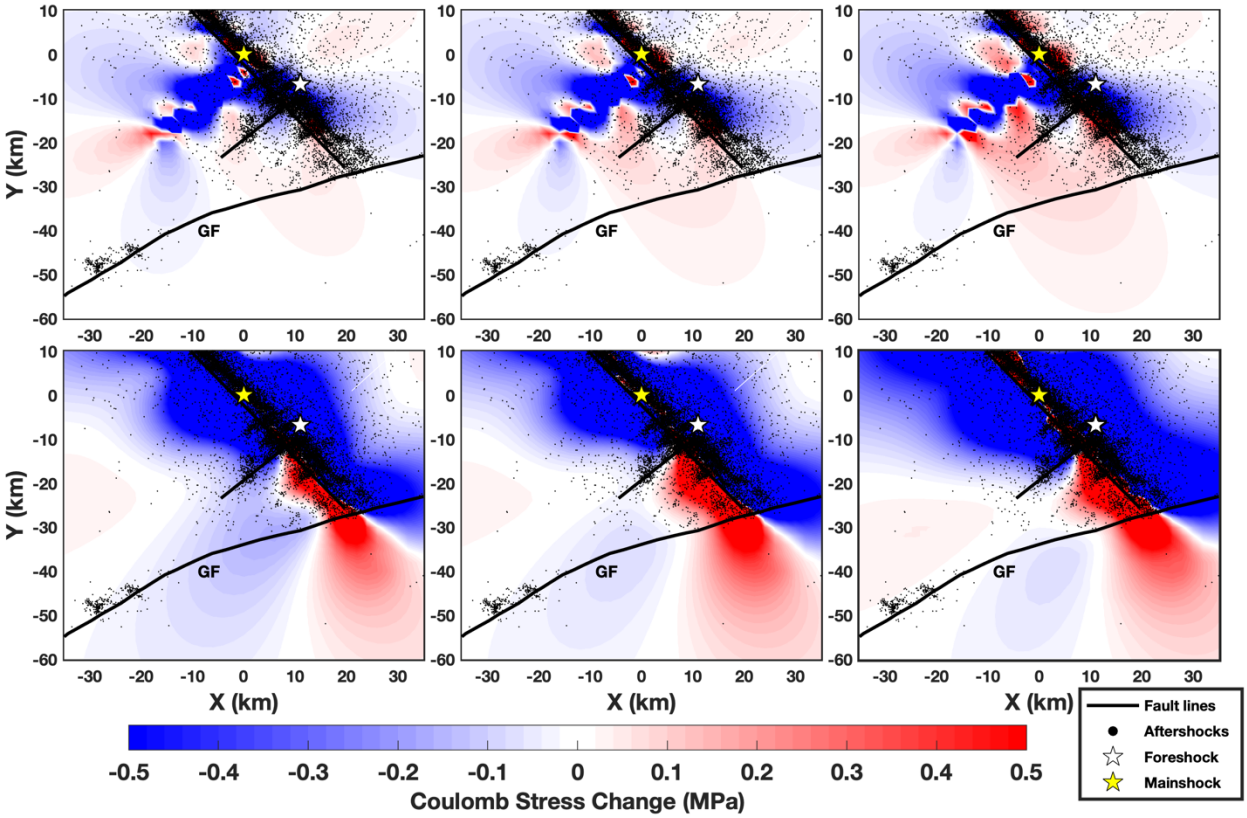

Figure 3. Coulomb stress change of the mainshock on a receiver fault of 70° strike and 90° dip, approximating the leftmost part of the Garlock fault in this figure. Top: Coulomb stress-change results for a 5 km depth source at friction coefficients of (left to right) 0.2, 0.4, and 0.6. Bottom: Coulomb stress-change results for a 10 km depth source with the same friction coefficients. The color version of this figure is available only in the electronic edition.

763
764
765

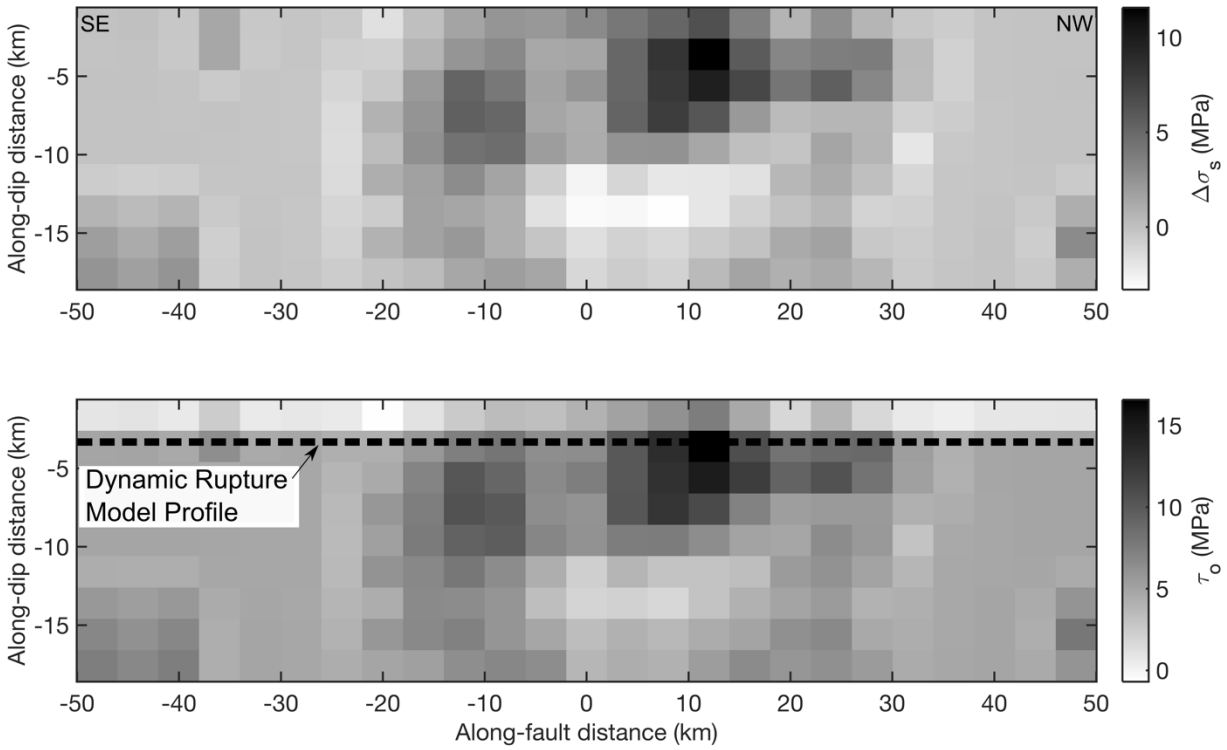

76(
767 **Figure 4.** Static stress-drop (top) and initial shear stress (bottom) along the mainshock fault plane.
768 Static stress-drop is calculated assuming a homogeneous, Poisson medium and initial shear stress
769 is computed using the complete stress-drop assumption. We select an initial shear stress profile
770 through the main asperity at 3 km depth (dashed line) for our 2-D dynamic rupture models.

771

772

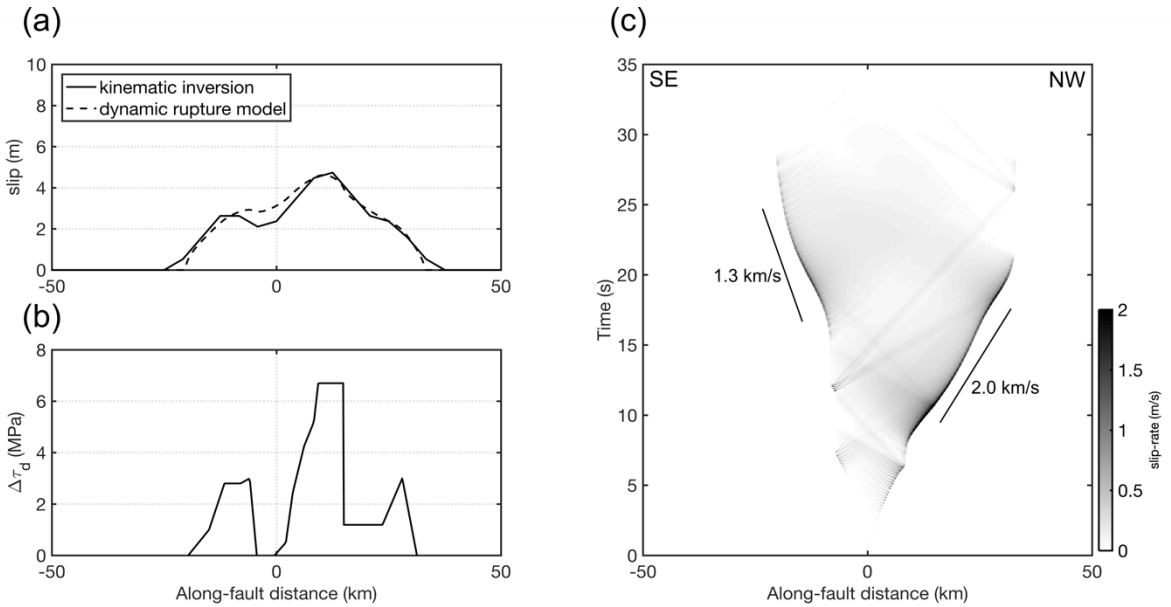

Figure 5. (a) Along-fault slip distribution resolved by the kinematic slip inversion (solid line) and that calculated from the dynamic rupture model (dashed line). The x-axis measures distance from where the earthquake is nucleated in our model. (b) Dynamic stress-drop along the fault. Location shown in fig 4. (c) Spatiotemporal and bilateral rupture history predicted by the dynamic rupture model. Solid lines signify average rupture front speed. Both rupture fronts propagate at sub-Rayleigh wave speed.

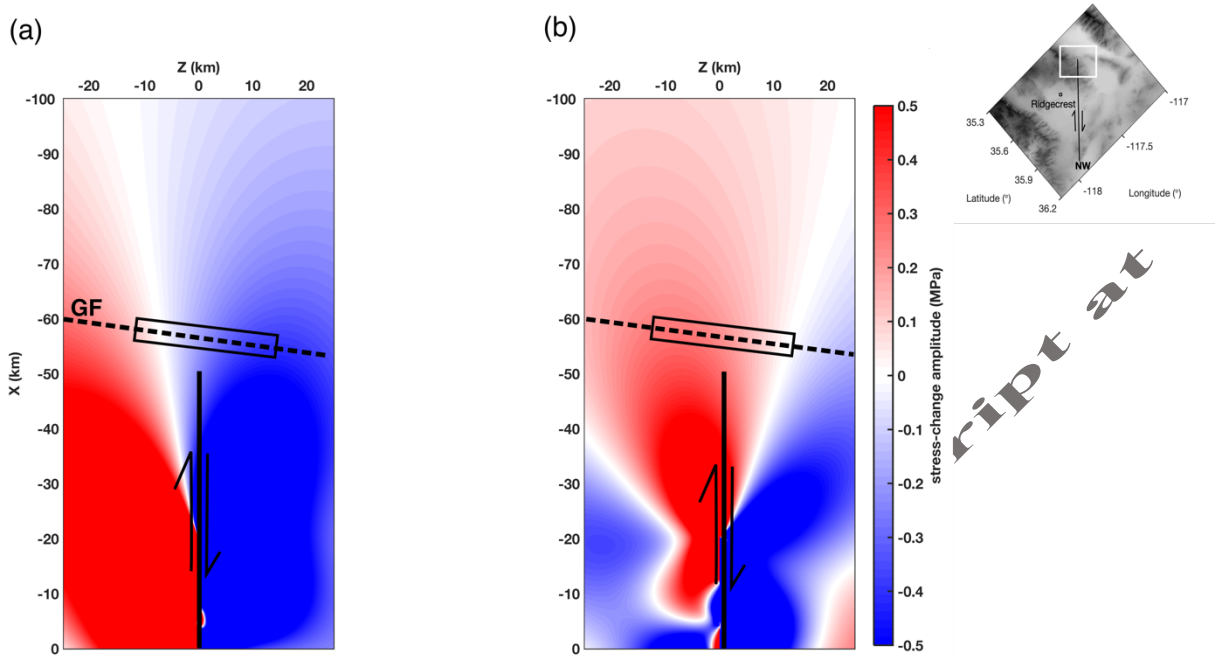

Figure 6. Static stress-change field in the modeling domain rotated to the strike of the Garlock fault. (a) normal stress and (b) shear stress. Garlock fault trace (dashed line) and Ridgecrest mainshock fault (solid line) are superimposed onto the figure. Box denotes approximate location of the creeping region (Barnhart et al., 2019). Spatial orientation is the same for figures 6 – 8. The color version of this figure is available only in the electronic edition.

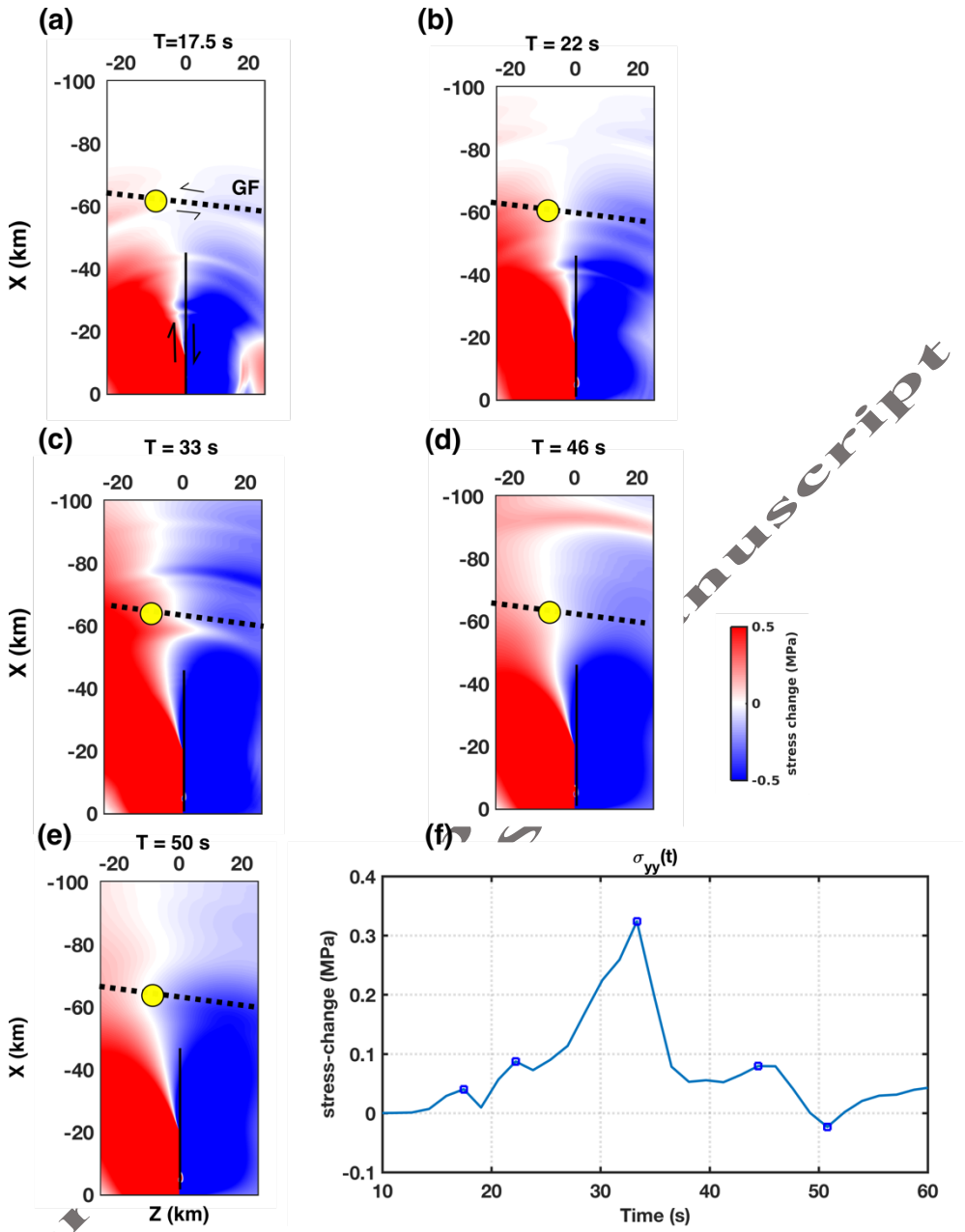

Figure 7. Normal stress changes (σ_{yy}) at various moments in time on the central Garlock fault during coseismic rupture of the mainshock. A point on the Garlock is selected to visualize the stress amplitude variability (solid circle). Subfigures (a) through (e) represent σ_{yy} from 17.5 to 50 seconds during rupture propagation. (f) shows the time-history of σ_{yy} where the blue squares denote the amplitude change at each of the normal stress snapshots (a-e). The color version of this figure is available only in the electronic edition.

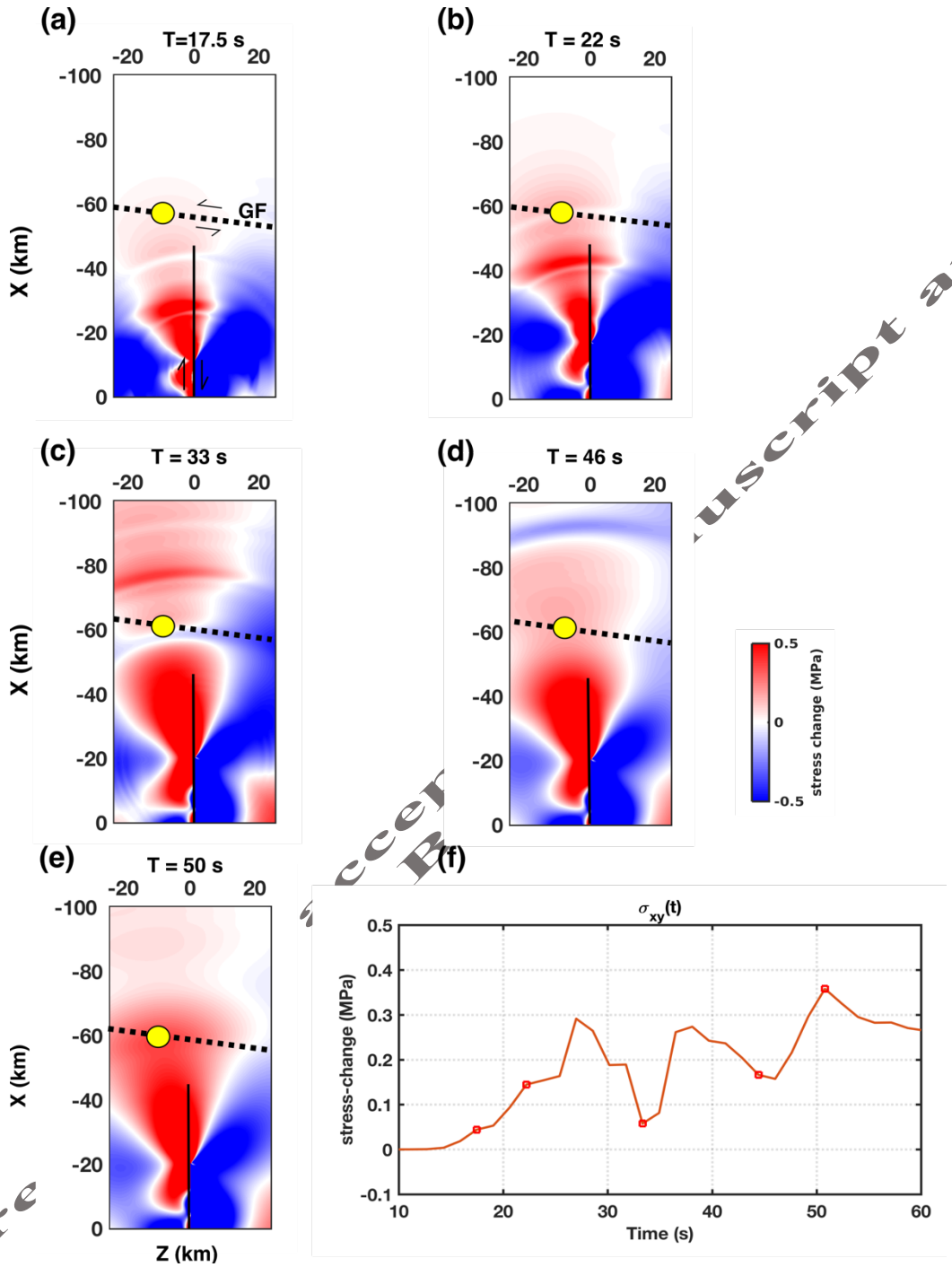

Figure 8. Similar to Fig. 9, but shear stress changes (σ_{xy}) during coseismic rupture. σ_{xy} exhibits three distinct peaks in its temporal stress-change on the Garlock fault at ~28, 38, and 50 seconds. The color version of this figure is available only in the electronic edition.

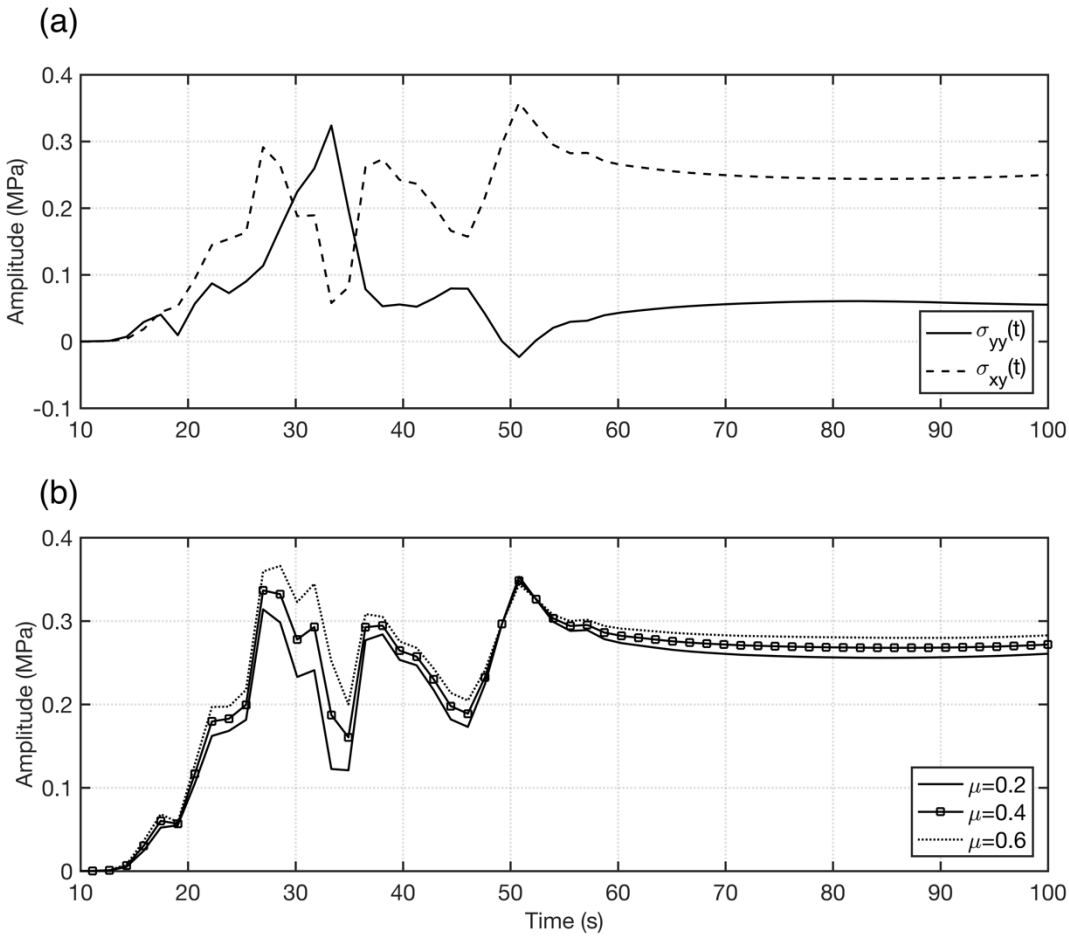

Figure 9. Stress change evolution on a section of the Garlock fault during the entire Ridgecrest earthquake simulation. (a) Normal (σ_{yy}) and shear (σ_{xy}) stress change. (b) Temporal Coulomb stress change for friction coefficient levels assessed in the static stress change analysis. Note that we plot the temporal stress change starting at 10 seconds because this is when the nucleation procedure ceases.